RSC Advances

PAPER

View Article Online
View Journal | View Issue

Cite this: *RSC Adv.*, 2023, **13**, 29944

$Ba_{2-x}Ho_xSr_{2-y}Ni_yFe_{12}O_{22}$ and its composite with MXene: synthesis, characterization and enhanced visible light mediated photocatalytic activity for colored dye and pesticide

Beriham Basha,[a] Alina Manzoor,[b] Z. A. Alrowaili,[c] Ayesha Ihsan, *[d] Imran Shakir[ef] and M. S. Al-Buriahi[g]

The rapid recombination of charges of photogenerated electrons and holes severely limits single semiconductor photocatalytic applications. In this study, a simple and facile sol–gel approach was used to synthesize $Ba_{2-x}Ho_xSr_{2-y}Ni_yFe_{12}O_{22}$ ($x = 0$, 0.1 and $y = 0$, 0.5). The composite of holmium–nickel doped barium–strontium ferrite with MXene ($Ba_{1.9}Ho_{0.1}Sr_{1.5}Ni_{0.5}Fe_{12}O_{22}$@MXene) was synthesized by ultrasonication method. These synthesized samples were subsequently used to photodegrade rhodamine B (RhB) and pendimethalin under visible light illumination. The results of the experiments demonstrated that MXene, as a cocatalyst, considerably reduces the rate of recombination of charges and broadens absorption of visible light by providing increased surface functional groups to improve the photocatalytic activity of synthesized samples. MXene is thermally stable, have high electrical conductivity, have adjustable bandgap, and hydrophilic in nature. The optimized $Ba_{1.9}Ho_{0.1}Sr_{1.5}Ni_{0.5}Fe_{12}O_{22}$@MXene composite demonstrated an excellent photocatalytic rate by degrading 78.88% RhB and 75.59% pendimethalin in 140 minutes. Moreover, the scavenging experiment revealed that photogenerated electrons and holes were the primary active species involved in RhB and pendimethalin photodegradation, respectively. $Ba_{1.9}Ho_{0.1}Sr_{1.5}Ni_{0.5}Fe_{12}O_{22}$@MXene showed increased photocatalytic behavior because it has increased surface area which decreases rate of recombination of electron and hole pair, hence photocatalytic activity increases. It is observed that $Ba_{1.9}Ho_{0.1}Sr_{1.5}Ni_{0.5}Fe_{12}O_{22}$@MXene has potential application in photocatalytic degradation of harmful pollutants.

Received 3rd September 2023
Accepted 5th October 2023

DOI: 10.1039/d3ra05993f

rsc.li/rsc-advances

1. Introduction

Grain yields have increased recently as a result of intensive farming methods. However, intensive agricultural techniques and overuse of agrochemicals have caused herbicide build-up in the soil, drinking water and groundwater.[1] Approximately 2 million tons of pesticides are being used annually worldwide and of which 47.5% are herbicides. The family of nitroaromatic compounds known as dinitroaniline herbicides include pendimethalin, nitralin, dinitramine, trifluralin *etc.* Dinitroanilines often reach the soil during agricultural applications and may also do so through surface runoff, groundwater discharge, field drainage, and spray drift as well as surface waters and sediments.[2] Dinitroaniline herbicide "pendimethalin" is widely used on a variety of crops, including cereals (wheat, barley, triticale, rye *etc.*), vegetables, potatoes, rice, legumes, maize, soybeans, nuts and fruits as well as ornamental plants and trees, to control grassy weed species and broadleaf weeds. Pendimethalin separates the chromosomes of harmful weeds and prevents their cell division and the formation of cell wall.[3] So, herbicide removal is one of the major and challenging tasks to prevent pollution of the environment. Some recent techniques for the removal of herbicides from polluted water include electrochemical oxidation, biological treatments, adsorption, photocatalysis and a combination of photocatalysis and ozonation.[4] Since many herbicides are stubborn pollutants, they must be eliminated.

Rhodamine B (RhB) is an organic dye, soluble in water and used in water tracing, fabric colouring, laser dyes, photosensitizers and fluorescent markers for microscopic structural

[a]*Department of Physics, College of Science, Princess Nourah Bint Abdulrahman University, P. O. Box 84428, Riyadh 11671, Saudi Arabia*
[b]*Department of Physics, Government College University Faisalabad, 38000, Punjab, Pakistan*
[c]*Department of Physics, College of Science, Jouf University, P. O. Box 2014, Sakaka, Saudia Arabia*
[d]*Institute of Chemistry, The Islamia University of Bahawalpur, Baghdad-ul-Jadeed Campus, Bahawalpur, 63100, Pakistan*
[e]*Department of Physics, Faculty of Science, Islamic University of Madinah, Madinah 42351, Saudi Arabia*
[f]*Department of Materials Science and Engineering, University of California, Los Angeles, USA*
[g]*Department of Physics, Sakarya University, Sakarya, Turkey*

testing. It is also used in biomedical research as a biological stain. Since it is carcinogenic in nature, its use in food processing is prohibited. Because of industrialization and unmonitored discharge of RhB, RhB severely contaminate fish and other species present in water that enters the food chain and have hazardous effects on humans and animals.[5]

Photocatalysis, which can result in the pollutant's total annihilation or mineralization, is an excellent choice for elimination of contaminants from waste water.[6,7] According to reports, semiconductor metal oxide photocatalysis is a remarkable green method for combating environmental pollution.[8] Ferrites, having excellent magnetic properties, have been studied and used for over 50 years.[9] The term "ferrite" is often used to describe a type of magnetic oxide compound having ferromagnetic characteristics that are found in powder or ceramic bodies and include a substantial amount of iron oxide. Ferrites are made up of transition metals and lanthanides especially chromium, iron and manganese. Their general formula is $M'M''_2O_4$, where M' is divalent metal cation (such as Mg^{2+}, Fe^{2+}, Cu^{2+}, Ni^{2+}, Zn^{2+}, and Co^{2+}) and M'' is trivalent metal ions (such as Fe^{3+}, Al^{3+}, Cr^{3+}, and Mn^{3+} *etc.*).[10] Ferrites are dark grey or black, hard and brittle oxide ceramics.[11] Iron ore magnetite (Fe_3O_4) is natural ferrite, having the chemical formula $Fe^{2+}Fe_2{}^{3+}O_4$. Its equivalent general formula is formulated as $Me^{2+}Fe_2{}^{3+}O_4$, here Me represents divalent metal cation (such as Cu, Mn, Co, Mg, Cd, Co, Ni, Zn *etc.*). The three forms of ferrites that may be distinguished by their crystal structures are spinel (MFe_2O_4), garnet ($M_3Fe_5O_{12}$), and hexagonal ($MFe_{12}O_{19}$), where M stands for divalent transition metal (Cu, Mn, Zn, Fe, Ni and Co).[12] While garnet and spinel are magnetically soft, hexagonal are hard. In the AO–Fe_2O_3–MeO system, hexagonal ferrites are a group of complex oxides, where A is Ca, Ba or Sr, *etc.*, and Me is Fe, Zn, Ni, Co, Cu or Mn, *etc.*[13] In the research labs of Philips, hexagonal ferrites were studied about 60 years ago.[14] The first magnetic mineral, magnetoplumbite, was given its name in 1925. In 1938, the $PbFe_{7.5}Mn_{3.5}Al_{0.5}Ti_{0.5}O_{19}$ crystal structure was identified. It was shown that $PbFe_{12}O_{19}$ made up the magnetoplumbite configuration in the simulation.[15] Magnetoplumbite are a class of magnetic oxides with hard magnetic characteristics and a hexagonal crystal structure. Recently, it was shown that several hexaferrites display single-phase multiferroic properties (materials with ferroelectric, ferroelastic, and ferromagnetic properties). Due to these characteristics, interest in hexagonal ferrites has grown significantly during the past years.[16] They are used in photocatalysis because of the light frequency they absorb for photocatalytic reaction and also due to their magnetic nature. They contain more catalytic sites which enhances their catalytic activity. They are used in degrading organic contaminants, dyes, CO_2, and as an antimicrobial agent.[17] Raut, S. S., *et al.*, reported the synthesis of $BaFe_{12}O_{19}$ nanoplatelets by molten salt method at various temperatures. Photocatalytic activity of synthesized nanoplatelets was studied by degrading hexahydro-1,3,5-trinitro-1,3,5 triazine (RDX) under UV and visible light. Photocatalytic degradation was less in visible region as compared to UV region. The synthesized nanoplatelets were magnetic in nature, has low bandgap (2.1 eV), easily separatable, reusable, and showed better activity than P25 TiO_2.[18] Bibi, I., *et al.*, synthesized Cr and Co doped $Ba_{1-x}Co_xFe_{12-y}Cr_yO_{19}$ nanoparticles by microemulsion method. The photocatalytic activity of synthesized nanoparticles was studied by using crystal violet dye under sunlight. The doped sample degraded 64.23% dye within 60 minutes.[19] Bibi, F., *et al.*, reported the synthesis of Nd and Cu doped $Ba_{1-x}Nd_xFe_{12-y}Cu_yO_{19}$ nanoparticles. Methylene green was used as a model pollutant to study the photocatalytic activity of synthesized samples. Undoped and co-doped sample degraded 37.4% and 92.6% dye, respectively. The increased activity is due to the formation of oxygen vacancies which reduces the rate of recombination of electron–hole pairs.[20] Doping with transition metals and rare earth metals is done to improve the catalytic activity of semiconductors. They reduce the bandgap energy, improve the light absorption ability and also increase the separation of charges.[21,22] Nickel is transition metal with an abundant electron shell structure. The incorporation of Ni into the semiconductor lattice would actively modify the physical properties of semiconductors by creating impurity energy level.[23] Rare earth metal ions have incompletely filled 4f and vacant 5d orbitals which often serve as a catalyst or promote catalysis.[24] Among all rare earth elements, holmium has one of the highest magnetic moments. Also, holmium oxide crystallizes in cubic structure which expose highly reactive base sites (O^{2-} and/or OH^-) and Lewis-acid sites. This OH^- may react with holes and generate hydroxyl radicals which improve the photocatalytic performance of semiconductors.[25]

MXene is a layered two-dimensional structure of transition metal, carbide or nitride. MXene have various properties such as high electrical conductivity, large surface area, wide interlayer spacing, more active sites and hydrophilicity.[26,27] MXene can help in removing heavy metals, radioactive nuclides and dyes.[28] In order to achieve better characteristics, MXene-based composites were also being investigated by scientists.[29–31] MXene serve as a 2D platform for the preparation of composite with photoactive semiconductors. MXene has negatively charged surface due to presence of surface functional groups which enables it to adsorb metal cations by electrostatic attractions and formation of semiconductors on MXene surface. MXene enhance the properties of semiconductors by facilitating separation of charge carriers in the composites and improve their photocatalytic activity. Favourable energy structure and high electrical conductivity of MXene enable it to trap and shuttle the photoelectrons generated from semiconductors thus promoting the charge-carriers separation and the photoactivity enhancement of MXene-based composites.[32,33] In current study, $Ba_{2-x}Ho_xSr_{2-y}Ni_yFe_{12}O_{22}$ ($x = 0$, 0.1 and $y = 0$, 0.5) have been synthesized by sol–gel method. Sol–gel method is a versatile method for synthesis of ferrites having many advantages such as high purity product is obtained at low temperature.[34] It is a low-cost method and no special instruments are needed. In this method, polycrystalline particles are prepared as homogeneous mixing of metal ions took place at molecular level. By adjusting various parameters *i.e.*, spin speed, nature and concentration of precursors, reaction time, calcination temperature *etc.*, the properties of synthesized samples can be controlled easily.[35] Another advantage of this method is that an active dopant is easily incorporated in sol during gelation step which allows the dopants to directly interact with metal ions and enhance their catalytic properties.[36] The composite of

$Ba_{2-x}Ho_xSr_{2-y}Ni_yFe_{12}O_{22}$ with MXene was synthesized by ultrasonication method. The photocatalytic activity of these synthesized materials was studied using rhodamine B dye and pendimethalin pesticide.

2. Experimental part

2.1. Chemicals

The chemicals used in the synthesis of materials were metal nitrates such as barium nitrate [$Ba(NO_3)_2$ (≥99%)], holmium nitrate [$Ho(NO_3)_3 \cdot 5H_2O$ (99.9%)], nickel nitrate [$Ni(NO_3)_2 \cdot 6H_2O$ (≥98.5%)], strontium nitrate [$Sr(NO_3)_2$ (≥99%)], iron nitrate [$Fe(NO_3)_3 \cdot 9H_2O$ (≥99.95%)], citric acid [$C_6H_8O_7 \cdot H_2O$ (99%)], MAX powder [Ti_3AlC_2 (≥90%)], hydrofluoric acid [HF], aqueous ammonia [NH_4OH] and deionized water. These chemicals were of analytical grade and used without further purification. All of these were brought from Sigma-Aldrich. The photocatalytic activity of samples was studied using rhodamine B dye and pendimethalin pesticide.

2.2. Synthesis of $Ba_2Sr_2Fe_{12}O_{22}$ and $Ba_{1.9}Ho_{0.1}Sr_{1.5}Ni_{0.5}Fe_{12}O_{22}$

Nickel nitrate, iron nitrate, barium nitrate, strontium nitrate, holmium nitrate, and citric acid were used in proper ratios to synthesize nickel and holmium substituted Ba–Sr hexagonal Y-type ferrites as given in Table 1. Samples with composition $x = 0$, 0.1 and $y = 0$, 0.5 were prepared by the sol–gel auto-combustion method by doping with different concentrations. Aqueous solutions of chemicals were prepared and stirred separately with the help of a magnetic stirrer. Then, all these separate solutions were mixed together and the resulting solution was stirred until a homogeneous solution was obtained. Ammonia solution was added dropwise to maintain pH at 7. After maintaining pH at 7, the solution was heated along with continuous stirring. After 4 hours of heating, xerogel was formed, which on further heating converted into ash. Then, ash was ground to obtain a fine powder using pestle mortar. Sintering of obtained powder was done for 6 hours at 950 °C. After sintering, again samples were ground to obtain fine powder. Fig. 1 shows the schematic diagram of synthesis of $Ba_{2-x}Ho_xSr_{2-y}Ni_yFe_{12}O_{22}$.

2.3. Synthesis of MXene (Ti_3C_2)

MAX powder (Ti_3AlC_2) was used as a precursor in the synthesis of MXene (Ti_3C_2). 1 g of MAX powder was dissolved in 20 ml hydrofluoric acid (40%, HF). This solution was magnetically stirred for 48 hours in a Teflon vessel for the etching of aluminium. De-ionized water was added to the resulting

Table 1 Concentration and weight of chemicals of $Ba_{2-x}Ho_xSr_{2-y}Ni_yFe_{12}O_{22}$

Composition	Barium nitrate g/5 ml	Holmium nitrate g/5 ml	Strontium nitrate g/5 ml	Nickel nitrate g/5 ml	Iron nitrate g/5 ml	Citric acid
$x = 0$ $y = 0$	2.614	0	2.117	0	24.24	3.1521 g/15 ml
$x = 0.1$ $y = 0.5$	2.483	0.221	1.587	0.727	24.24	5.2537 g/25 ml

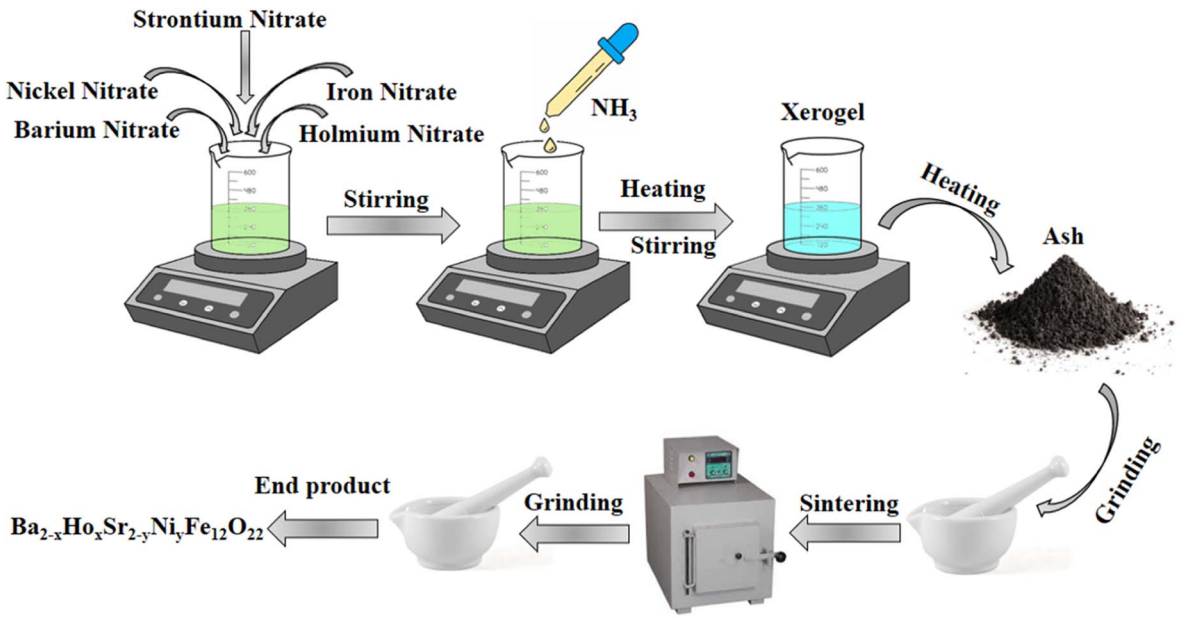

Fig. 1 Schematic diagram of synthesis of $Ba_{2-x}Ho_xSr_{2-y}Ni_yFe_{12}O_{22}$.

black-coloured sample and centrifugation was done at 5500 rpm for 10 minutes. Washing of the sample was done until pH became neutral. At last, the sample was dried in the oven at 60 °C.

2.4. Synthesis of composite with MXene

Ultrasonication method was used to prepare a composite of $Ba_{1.9}Ho_{0.1}Sr_{1.5}Ni_{0.5}Fe_{12}O_{22}$ with MXene. At first, separate solutions of $Ba_{1.9}Ho_{0.1}Sr_{1.5}Ni_{0.5}Fe_{12}O_{22}$ and MXene were prepared in distilled water in ratio 9 : 1. These solutions were sonicated for 2 hours and stirred for 1 hour to prepare a homogeneous mixture. Then, both solutions were mixed and sonicated for 3 hours to obtain a homogeneous sample solution. The sample solution obtained was then dried in an oven at 80 °C and the obtained sample was ground to make a fine powder of $Ba_{1.9}Ho_{0.1}Sr_{1.5}Ni_{0.5}Fe_{12}O_{22}$@MXene composite.

2.5. Photocatalytic activity

The photocatalytic behaviour of synthesized materials was investigated by photodegrading aqueous solutions of rhodamine B dye and pendimethalin pesticide which were taken as model pollutants. This experiment was performed in two light bulbs of 200 W each. A 7 ppm solution of rhodamine B dye and 0.6 ppm solution of pendimethalin was prepared in distilled water and 500 ml of each was taken in separate beakers. 30 mg of each synthesized photocatalyst was added to these beakers and stirring was done in dark for 1 hour to achieve adsorption–desorption equilibrium. About 5 ml of sample solutions were taken from the reaction mixture. Then, the apparatus was kept in a bulb and sample solutions were obtained at regular time intervals (20 min), centrifuged and absorbance was noted using UV-vis spectrophotometer. The absorbance of both dye and pesticide was noted by the same procedure.

Rhodamine B shows absorbance peaks at approximately 553 nm. It was observed that the intensity of characteristic absorbance peaks of rhodamine B decreased and eventually faded with the time. It was noted that bare material took greater time in photodegradation as compared to the time taken by composite with MXene.[5]

By utilizing the following formula percentage degradation is calculated:

$$\text{Degradation percentage} = 100\left(1 - \frac{C_t}{C_o}\right) \quad (1)$$

The starting concentration of organic dyes at time 0 min is denoted by C_o, while the concentration at time t min is denoted by C_t.[37]

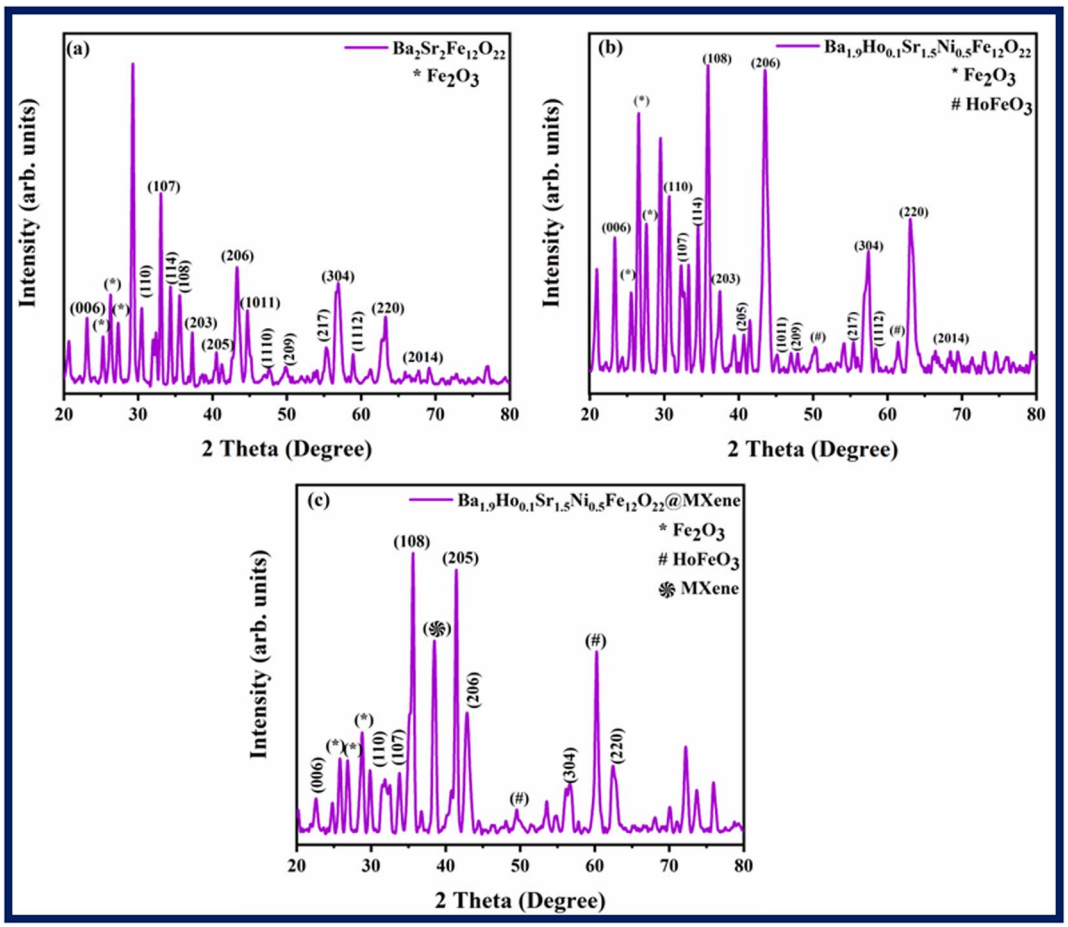

Fig. 2 XRD patterns of (a) $Ba_2Sr_2Fe_{12}O_{22}$ (b) $Ba_{1.9}Ho_{0.1}Sr_{1.5}Ni_{0.5}Fe_{12}O_{22}$, and (c) $Ba_{1.9}Ho_{0.1}Sr_{1.5}Ni_{0.5}Fe_{12}O_{22}$@MXene.

3. Characterization

Different techniques were used to determine the structural characteristics and properties of prepared materials. Shimadzu 6100AS XRD diffractometer, using Cu Kα radiation source (λ = 1.5418 Å), was used to identify the phases of synthesized samples. Shimadzu IR Affinity-IS spectrometer was used to examine Fourier transform infrared spectra in the range of 4000 cm^{-1} to 400 cm^{-1}. The morphology of synthesized samples was determined by thermal emission scanning electron microscope. Using an Agilent Cary 60 spectrophotometer, UV-visible spectra of the samples was obtained.

4. Result and discussions

4.1. XRD analysis

X-ray diffraction (XRD) was used to characterize the structural characteristics of $Ba_{2-x}Ho_xSr_{2-y}Ni_yFe_{12}O_{22}$ (where x = 0, 0.1 and y = 0, 0.5) and the associated XRD patterns are shown in Fig. 2. Bragg's reflection peaks were observed at different 2θ values *i.e.*, 23.105° (006), 30.43° (110), 32.99° (107), 34.28° (114), 35.56° (108), 37.19° (203), 40.45° (205), 43.24° (206), 44.63° (1011), 47.55° (1110), 49.87° (209), 55.34° (217), 56.86° (304), 58.96° (1112), 63.26° (220), 67.66° (2014). These reflection peaks are well-matched with the standard JCPDS card number (80-1198). XRD data confirmed the successful synthesis of hexagonal shaped ferrites.[38] Distinct and sharp peaks indicate high crystallinity and purity of phases. Bragg's reflection peaks observed at 2θ values *i.e.*, 25.19°, 26.25°, 27.18° in Fig. 2a and Bragg's reflection peaks at 25.46°, 26.518° and 27.55° in Fig. 2b correspond to the secondary phases of Fe_2O_3. Peaks at 50.29° and 61.48° in Fig. 2b correspond to $HoFeO_3$.

Ionic radii and electronic configuration are significant variables that can have an impact on structural characteristics. The formation of the secondary phase is subsequently caused by the greater concentration of ions of rare earth elements at tetrahedral and octahedral sites. A secondary phase (impurity) formed on the surface of grain boundary as shown in the XRD patterns by "*, #" caused deformation in the lattice inside the grain regions. This deformation in lattice may be caused by internal stress brought on by the different thermal expansion coefficients of the bulk material and the inter-granular material, or it might be caused by a mismatch in the lattice at the boundary/grain interface.[39] These secondary phase peaks (Fe_2O_3) are well-matched to the JCDPS card number (89-0599). The $Ba_{1.9}Ho_{0.1}Sr_{1.5}Ni_{0.5}Fe_{12}O_{22}$@MXene spectra in Fig. 2c showed a prominent characteristic peak of MXene at 2θ = 38° (104) which confirmed the presence of MXene in the $Ba_{1.9}Ho_{0.1}Sr_{1.5}Ni_{0.5}Fe_{12}O_{22}$@MXene composite.[40]

$Ba_2Sr_2Fe_{12}O_{22}$ and $Ba_{1.9}Ho_{0.1}Sr_{1.5}Ni_{0.5}Fe_{12}O_{22}$ crystal size was determined Debye and Scherrer formula which is as follows.[41–43]

$$D = \frac{0.9\lambda}{\beta \cos \theta} \quad (2)$$

where D is the crystallite size, λ is the X-ray wavelength, β stands for full width at half maximum (FWHM) and θ is Bragg's diffraction angle. $Ba_2Sr_2Fe_{12}O_{22}$, and $Ba_{1.9}Ho_{0.1}Sr_{1.5}Ni_{0.5}Fe_{12}O_{22}$ have average crystallite sizes of 19.2645 nm, and 14.46 nm, respectively (Table 2).

Table 2 XRD parameters of $Ba_2Sr_2Fe_{12}O_{22}$ and $Ba_{1.9}Ho_{0.1}Sr_{1.5}Ni_{0.5}Fe_{12}O_{22}$

	$Ba_2Sr_2Fe_{12}O_{22}$	$Ba_{1.9}Ho_{0.1}Sr_{1.5}Ni_{0.5}Fe_{12}O_{22}$
Crystallite size	19.2645 nm	14.46 nm
Dislocation density	0.00269 nm^{-2}	0.00478 nm^{-2}
Space group	$P6_3/mmc$	—
Crystal system	Hexagonal	Hexagonal
Cell constant	$a = b$ = 5.849 (Å)	$a = b$ = 5.843 (Å)
	c = 23.38 (Å)	c = 23.21 (Å)
Volume (Å^3)	692.66 Å^3	686.24 Å^3

The dislocation density of prepared samples was found by following formula:

$$\delta = \frac{1}{D^2} \quad (3)$$

Here, δ is the dislocation density and D is the crystallite size of synthesized materials.

The lattice constants of hexagonal cell was calculated using cell software. The volume of hexagonal crystal system was calculated by the following equation:

$$\text{Volume} = abc(1 - \cos^2\alpha - \cos^2\beta - \cos^2\gamma + 2\cos\alpha\beta\gamma)^{1/2} \quad (4)$$

(where $\alpha = \beta = 90°$ and $\gamma = 120°$ for hexagonal system).

4.2. FT-IR

FT-IR spectra of all synthesized samples *i.e.*, $Ba_2Sr_2Fe_{12}O_{22}$, $Ba_{1.9}Ho_{0.1}Sr_{1.5}Ni_{0.5}Fe_{12}O_{22}$, and $Ba_{1.9}Ho_{0.1}Sr_{1.5}Ni_{0.5}Fe_{12}O_{22}$@MXene are shown in Fig. 3 in the range of 400 cm^{-1} to 4000 cm^{-1}. FT-IR analysis was done to analyse structural

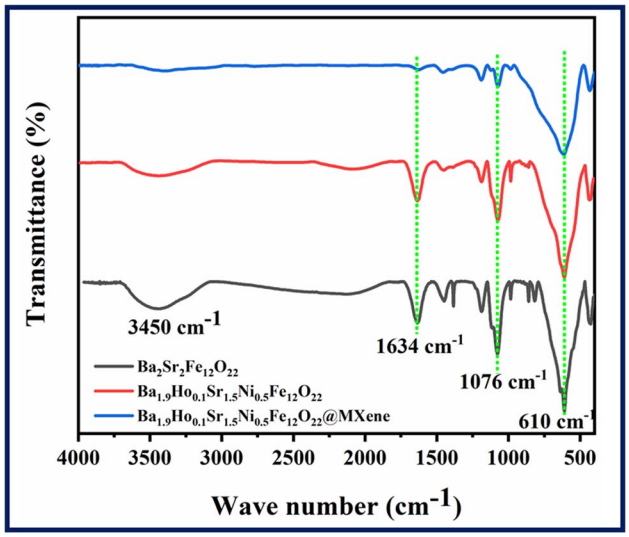

Fig. 3 FTIR spectra of $Ba_2Sr_2Fe_{12}O_{22}$, $Ba_{1.9}Ho_{0.1}Sr_{1.5}Ni_{0.5}Fe_{12}O_{22}$, and $Ba_{1.9}Ho_{0.1}Sr_{1.5}Ni_{0.5}Fe_{12}O_{22}$@MXene.

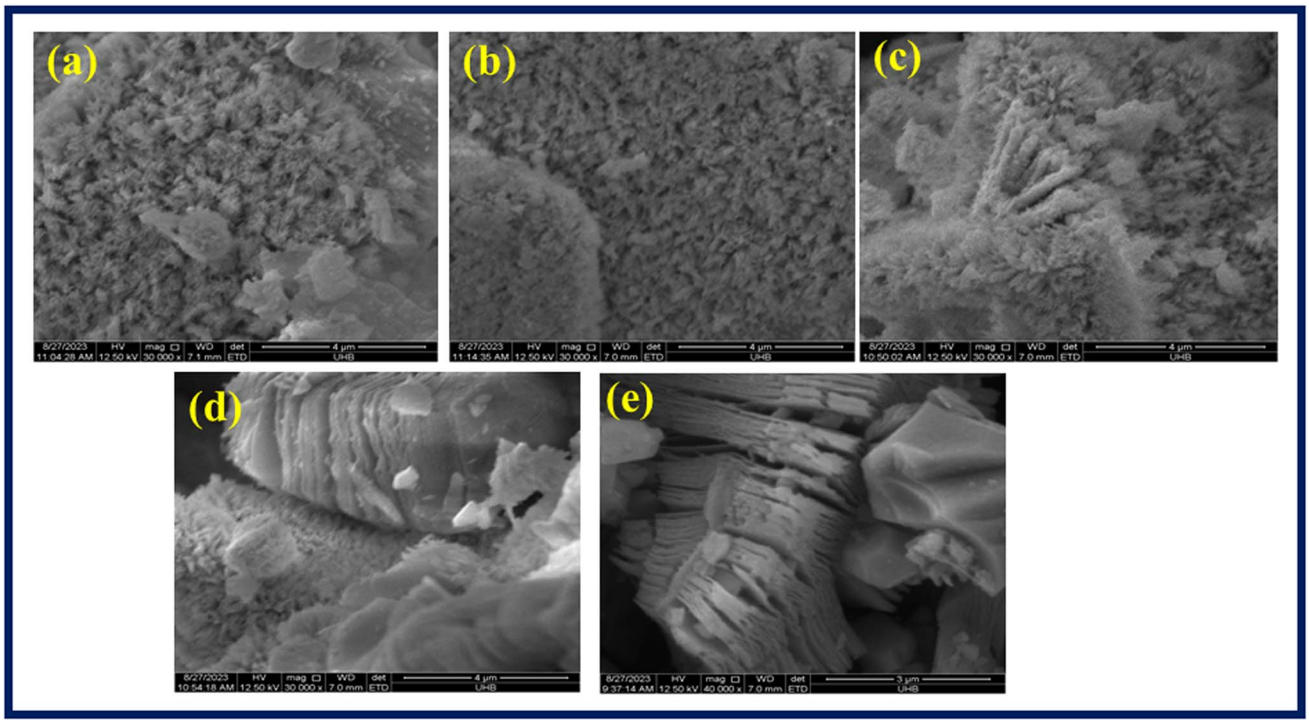

Fig. 4 SEM images of (a) $Ba_2Sr_2Fe_{12}O_{22}$ (b) $Ba_{1.9}Ho_{0.1}Sr_{1.5}Ni_{0.5}Fe_{12}O_{22}$, (c and d) $Ba_{1.9}Ho_{0.1}Sr_{1.5}Ni_{0.5}Fe_{12}O_{22}$@MXene and (e) MXene.

information and functional group of synthesized materials. The frequency band that appeared at 610 cm^{-1} is due to intrinsic stretching vibrations of tetrahedral and octahedral site of barium hexaferrite structure.[44] Ferrite formation is confirmed by the absorption of infra-red radiation in this region.[45,46] The variation in low and high frequency bands indicated that holmium and nickel were incorporated into the matrix of barium–strontium ferrites.[47,48] The relative peaks appeared at 1634 cm^{-1} and 3450 cm^{-1} are due to stretching vibrations of water molecules.[49] The decrease in intensity of peaks in the FTIR spectrum of doped and composite samples confirmed the synthesis of $Ba_{1.9}Ho_{0.1}Sr_{1.5}Ni_{0.5}Fe_{12}O_{22}$, and $Ba_{1.9}Ho_{0.1}Sr_{1.5}Ni_{0.5}Fe_{12}O_{22}$@MXene samples.

4.3. Scanning electron microscopy

Scanning electron microscopy was performed to evaluate the morphology of synthesized samples. Fig. 4a–e showed SEM images of prepared $Ba_2Sr_2Fe_{12}O_{22}$, $Ba_{1.9}Ho_{0.1}Sr_{1.5}Ni_{0.5}Fe_{12}O_{22}$, $Ba_{1.9}Ho_{0.1}Sr_{1.5}Ni_{0.5}Fe_{12}O_{22}$/MXene, and bare MXene, respectively. The SEM images were taken at different magnifications.

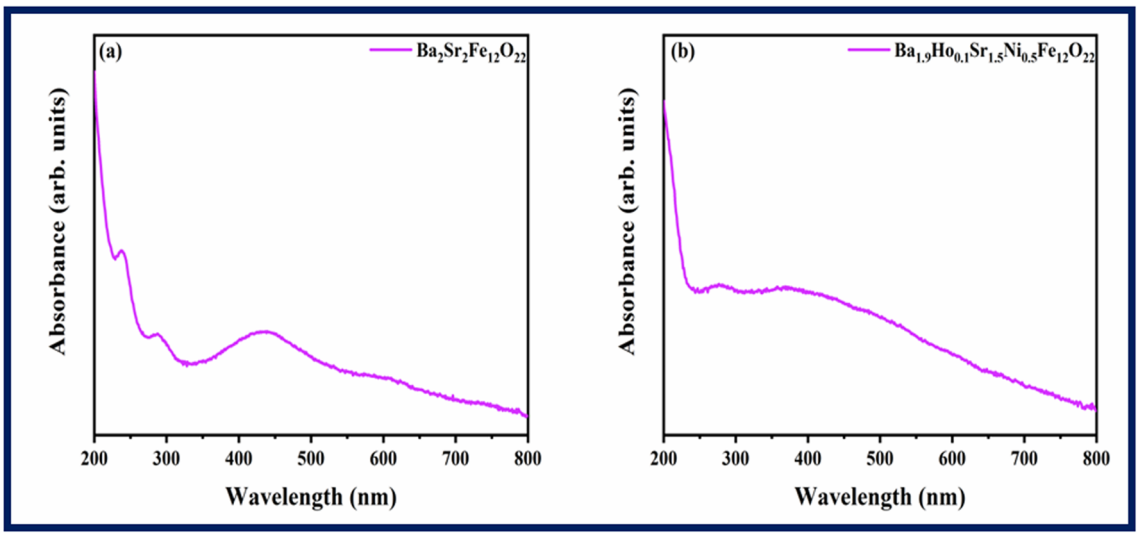

Fig. 5 Absorption spectra of (a) $Ba_2Sr_2Fe_{12}O_{22}$ (b) $Ba_{1.9}Ho_{0.1}Sr_{1.5}Ni_{0.5}Fe_{12}O_{22}$.

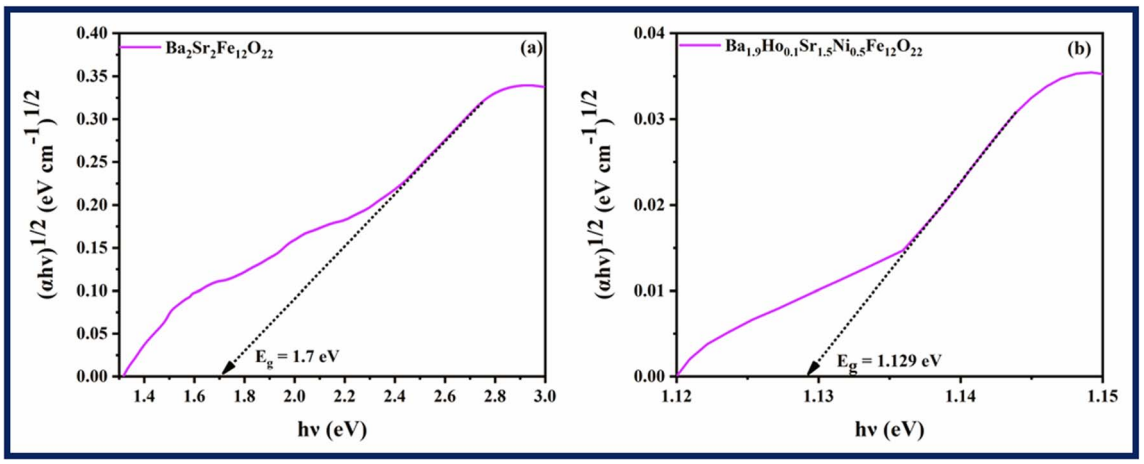

Fig. 6 Tauc plots of (a) $Ba_2Sr_2Fe_{12}O_{22}$ (b) $Ba_{1.9}Ho_{0.1}Sr_{1.5}Ni_{0.5}Fe_{12}O_{22}$.

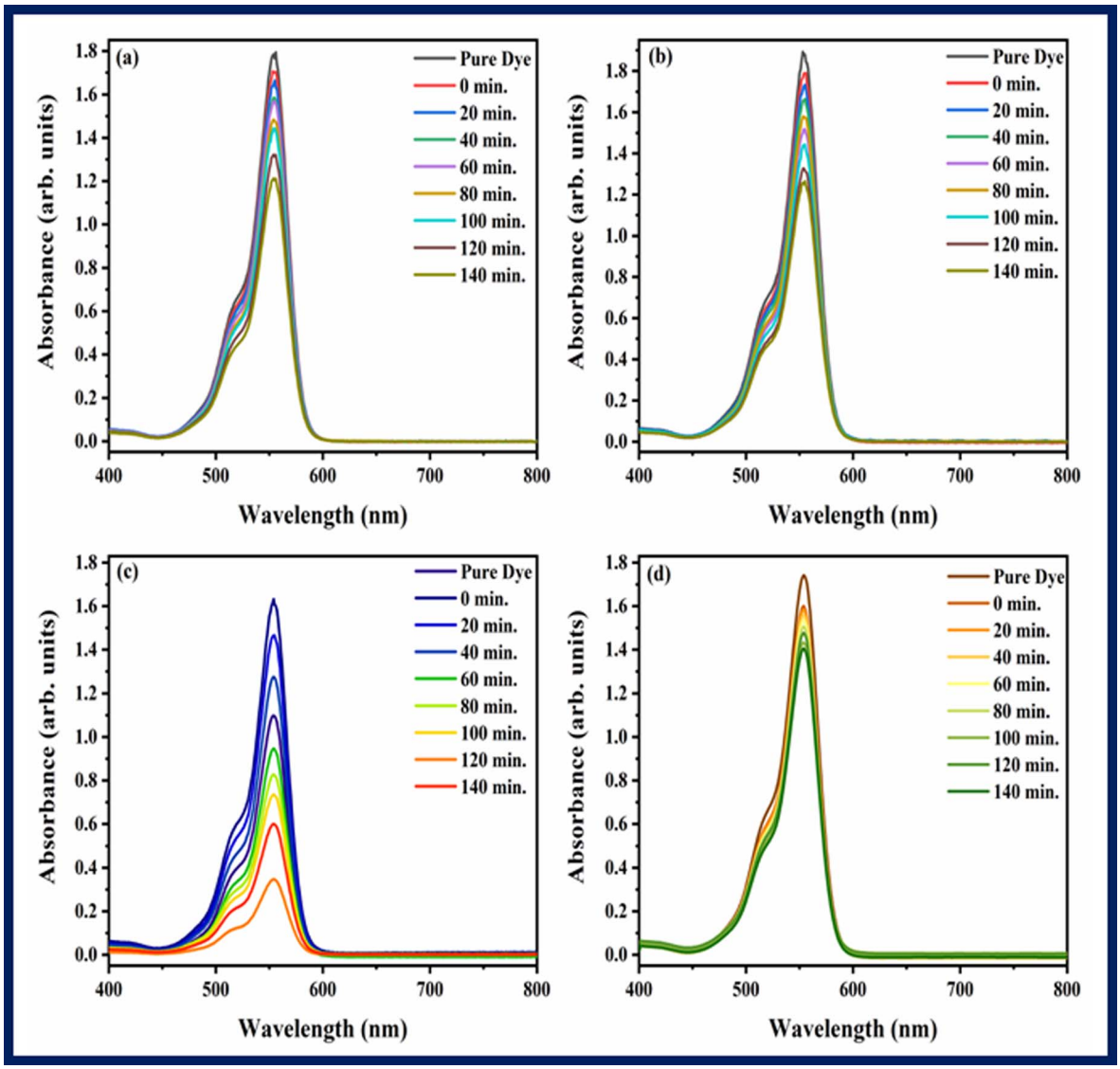

Fig. 7 Photodegradation spectra of rhodamine B using (a) $Ba_2Sr_2Fe_{12}O_{22}$ (b) $Ba_{1.9}Ho_{0.1}Sr_{1.5}Ni_{0.5}Fe_{12}O_{22}$, (c) $Ba_{1.9}Ho_{0.1}Sr_{1.5}Ni_{0.5}Fe_{12}O_{22}$@MXene, and (d) MXene.

The SEM images (Fig. 4a) revealed that the synthesized $Ba_2Sr_2Fe_{12}O_{22}$ structures have flakes like morphology. In the case of $Ba_{1.9}Ho_{0.1}Sr_{1.5}Ni_{0.5}Fe_{12}O_{22}$, no significant alteration in the morphology was observed. The SEM image of $Ba_{1.9}Ho_{0.1}Sr_{1.5}Ni_{0.5}Fe_{12}O_{22}$/MXene [Fig. 4c and d] showed that synthesized particles are intercalated in MXene sheets as both flakes and MXene sheets were observed. Accordion like structure comprised of 2D sheets of MXene was observed in SEM image of pure MXene in Fig. 4e. This confirmed the successful synthesis of MXene. The average grain size of $Ba_2Sr_2Fe_{12}O_{22}$ and $Ba_{1.9}Ho_{0.1}Sr_{1.5}Ni_{0.5}Fe_{12}O_{22}$, was calculated using ImageJ software and found to be approximately 26.8 μm and 24.7 μm, respectively.

4.4. UV-vis analysis

UV-vis spectra of $Ba_2Sr_2Fe_{12}O_{22}$ and $Ba_{1.9}Ho_{0.1}Sr_{1.5}Ni_{0.5}Fe_{12}O_{22}$ was measured in the range of 200 nm to 800 nm, and the results are displayed in Fig. 5.

The efficiency of synthesized samples was analysed by finding their bandgap energy. Bandgap significantly influences the generation of electron–hole pairs in conduction and valence band. Tauc plots (Fig. 6) are used to calculate the band gap energy using eqn (5) below.

$$(\alpha\hbar\nu)^n = \beta(\hbar\nu - E_g) \quad (5)$$

in this formula, α stands for the absorption coefficient, ν for the frequency of the light being employed, $\hbar$ for Planck's constant, n stands for either direct (2) or indirect bandgap (1/2), and β for the proportionality constant. According to Fig. 6, the estimated optical band gaps (E_g) for $Ba_2Sr_2Fe_{12}O_{22}$ and $Ba_{1.9}Ho_{0.1}Sr_{1.5}Ni_{0.5}Fe_{12}O_{22}$ are 1.7 eV and 1.129 eV, respectively. It shows that the band-gap of $Ba_2Sr_2Fe_{12}O_{22}$ is reduced by doping of holmium and nickel. Additionally, the $Ba_{1.9}Ho_{0.1}Sr_{1.5}Ni_{0.5}Fe_{12}O_{22}$ band-gap decreases to a lower value, confirming the electronic interaction of holmium and nickel in $Ba_2Sr_2Fe_{12}O_{22}$.

5. Photocatalysis

The ability of photocatalysts to degrade rhodamine B and pendimethalin was assessed under the influence of visible light. Fig. 7 and 8 showed the spectra of photodegradation of rhodamine B and pendimethalin, respectively. Photocatalysis is based on three phases. Photons with energies higher than the synthesized samples' bandgap energy are absorbed in the first step. In the following step, electrons and holes are produced and transferred. On the photocatalyst surface, reduction and

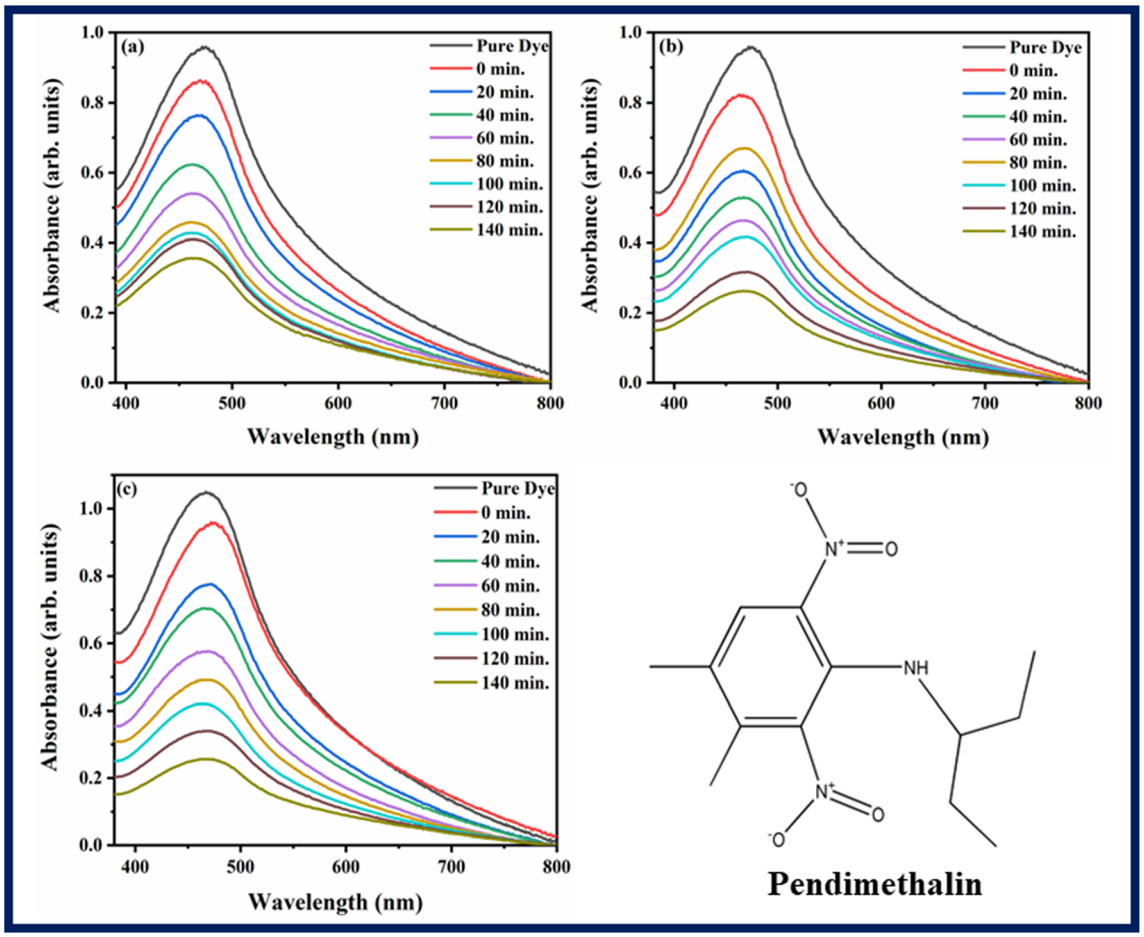

Fig. 8 Photodegradation spectra of pendimethalin using (a) $Ba_2Sr_2Fe_{12}O_{22}$, (b) $Ba_{1.9}Ho_{0.1}Sr_{1.5}Ni_{0.5}Fe_{12}O_{22}$, and (c) $Ba_{1.9}Ho_{0.1}Sr_{1.5}Ni_{0.5}Fe_{12}O_{22}$@MXene.

oxidation take place in the third stage. After various reaction times, the maximum absorption of dye and pesticide gradually diminished, as seen in Fig. 7 and 8. $Ba_2Sr_2Fe_{12}O_{22}$ has a very low degradation efficiency for RhB under the influence of visible light. However, as shown in Fig. 7c and 8c, the proportion of RhB and pendimethalin that was photo-catalytically degraded by the composite with MXene was around 78.88% and 75.59% in 140 minutes, respectively. The surface area of the photo-catalyst increases with the composite formation with MXene, that's why maximum absorbance occurred and the rate of electron–hole pair recombination decreased.

Using pseudo-first-order kinetic eqn (6), the rate of photo-degradation of RhB dye and pendimethalin was investigated.

$$-\ln \frac{C_t}{C_o} = Kt \quad (6)$$

in this equation, K and t stand for pseudo-first-order reaction rate constant and irradiation time, respectively. Fig. 9 and 10 showed the kinetics graphs for degradation of rhodamine B and pendimethalin, respectively. Slope of the line of $\ln \frac{C_t}{C_o} vs.t$ represents the rate constant. It was discovered that the kinetic rate constant of the $Ba_{1.9}Ho_{0.1}Sr_{1.5}Ni_{0.5}Fe_{12}O_{22}$ composite is greater than that of $Ba_2Sr_2Fe_{12}O_{22}$. The value of rate constant was also found using eqn (4) as shown in Fig. 9d and 10d. Using MXene, $Ba_2Sr_2Fe_{12}O_{22}$, $Ba_{1.9}Ho_{0.1}Sr_{1.5}Ni_{0.5}Fe_{12}O_{22}$ and $Ba_{1.9}Ho_{0.1}Sr_{1.5}Ni_{0.5}Fe_{12}O_{22}$@MXene the rate constant for degradation of rhodamine B was 0.00108 min^{-1}, 0.00223 min^{-1}, 0.00455 min^{-1}, and 0.00737 min^{-1} respectively and the rate constant for the degradation of pendimethalin was 0.00643 min^{-1}, 0.00779 min^{-1} and 0.0086 min^{-1}, respectively. It showed that $Ba_{1.9}Ho_{0.1}Sr_{1.5}Ni_{0.5}Fe_{12}O_{22}$@MXene has highest rate of degradation of rhodamine B and pendimethalin. Percentage degradation of rhodamine B (Fig. 9c) in bulb using pure MXene, $Ba_2Sr_2Fe_{12}O_{22}$, $Ba_{1.9}Ho_{0.1}Sr_{1.5}Ni_{0.5}Fe_{12}O_{22}$ and $Ba_{1.9}Ho_{0.1}Sr_{1.5}Ni_{0.5}Fe_{12}O_{22}$@MXene was 16.84%, 41.56%, 55.86%, and 78.88%, respectively. Percentage degradation of pendimethalin (Fig. 10c) in bulb using $Ba_2Sr_2Fe_{12}O_{22}$,

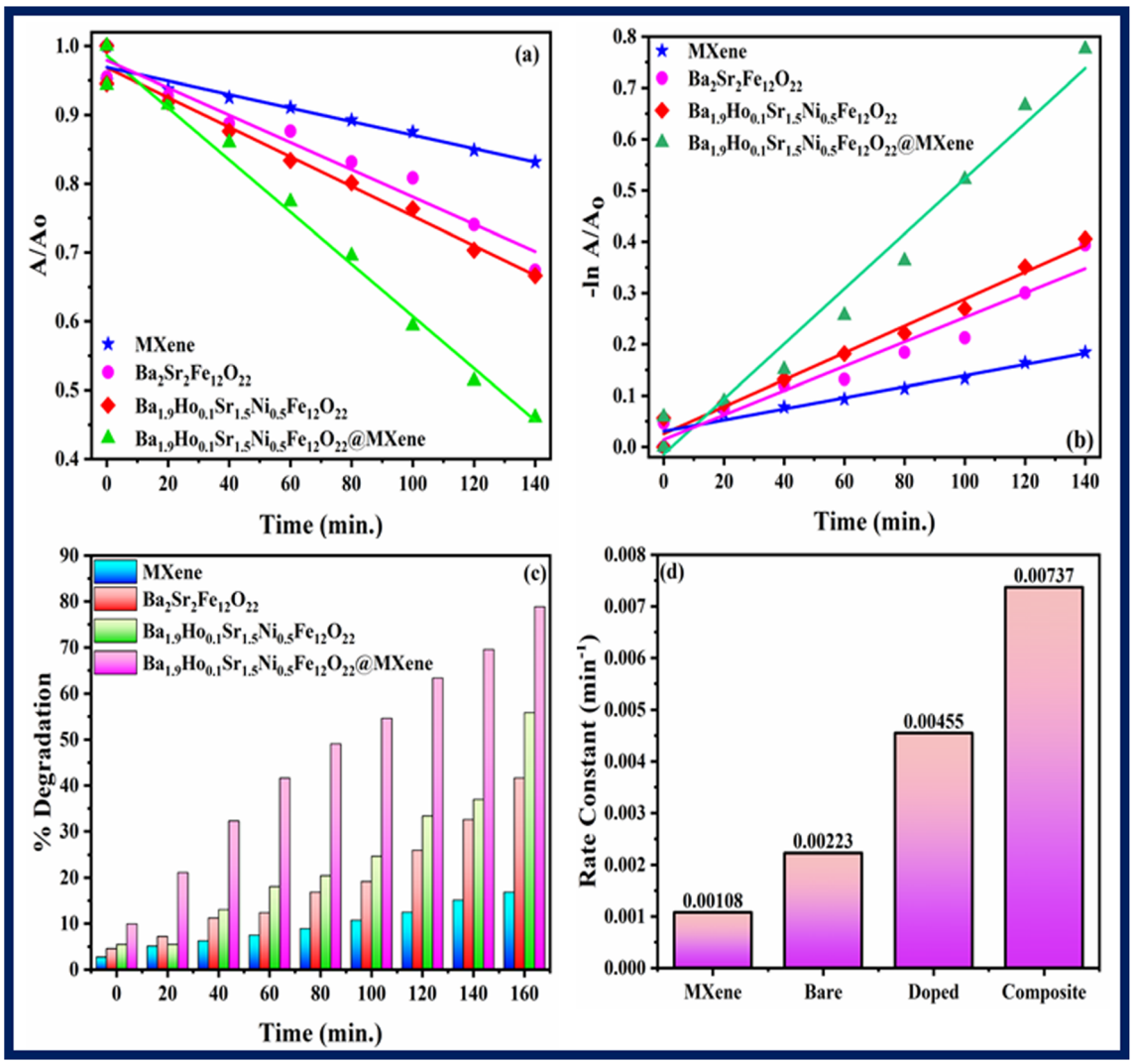

Fig. 9 Kinetic study of all synthesized samples using rhodamine B (a) kinetic rate (b) linear kinetics (c) percentage degradation (d) rate constant.

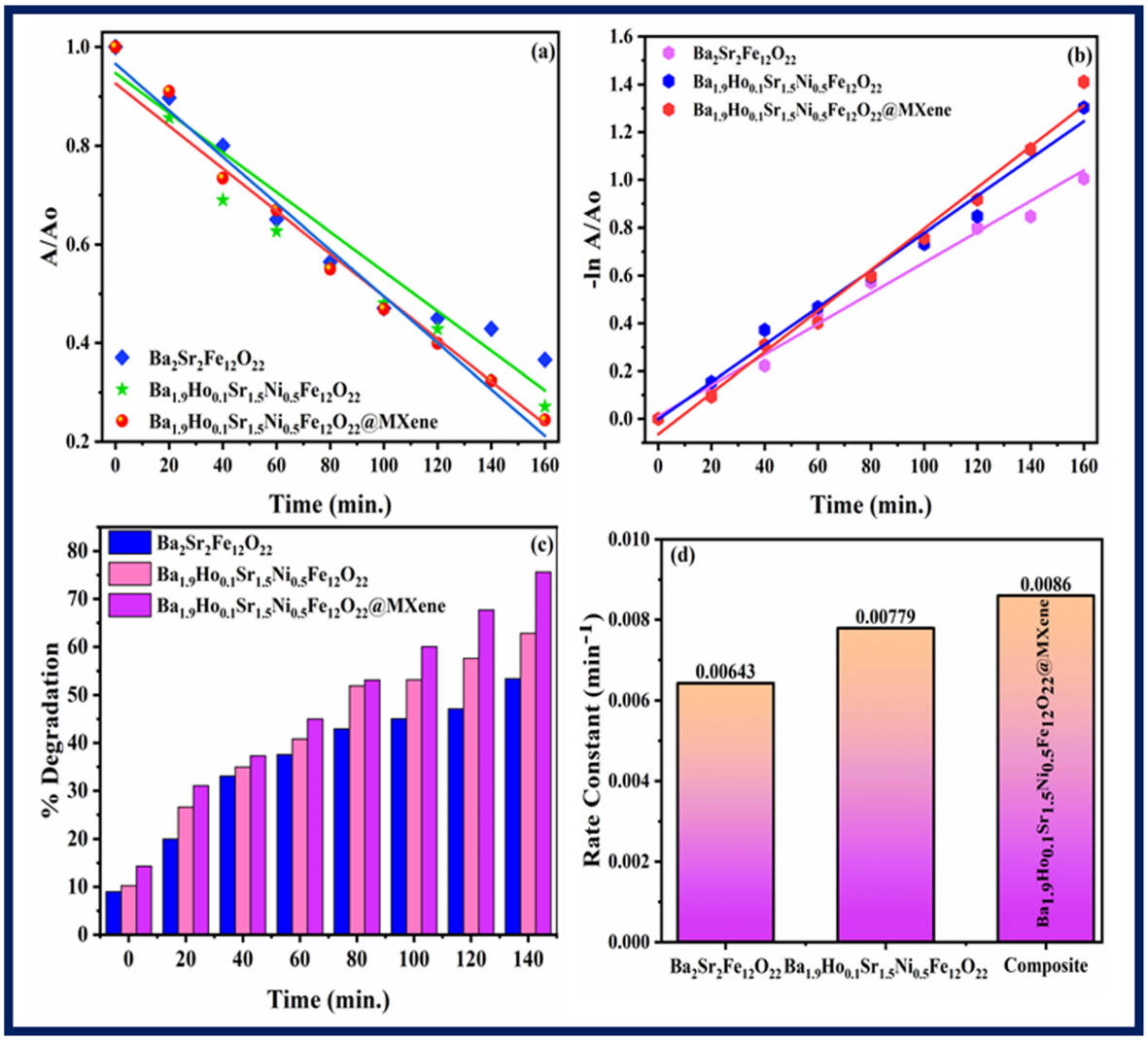

Fig. 10 Kinetic study of all synthesized samples using pendimethalin (a) kinetic rate (b) linear kinetics (c) percentage degradation (d) rate constant.

$Ba_{1.9}Ho_{0.1}Sr_{1.5}Ni_{0.5}Fe_{12}O_{22}$, and $Ba_{1.9}Ho_{0.1}Sr_{1.5}Ni_{0.5}Fe_{12}O_{22}$@-MXene was 53.389%, 62.83% and 75.59%, respectively.

For investigation of degradation mechanism for photocatalytic activity, following equations are used for calculation of valence band potential (E_{VB}) and conduction band potential (E_{CB}):[50]

$$E_{VB} = X - E_e + \tfrac{1}{2}E_g \quad (7)$$

$$E_{CB} = E_{VB} - E_g \quad (8)$$

Here X is the absolute electronegativity value, E_e is the free electron energy (4.5 eV relative to NHE) and E_g is the bandgap energy of synthesized semiconductor. The calculated values of E_{VB} and E_{CB} are −2.5765 eV and −3.7055 eV, respectively.[51]

To facilitate the reduction and oxidation processes, photocatalysts use light energy. When light is illuminated on a photocatalyst, the valence electrons of the photocatalyst are excited into conduction band. As a result, electron–hole pairs are created, which are then in charge of causing reduction and oxidation processes. When holes oxidize H_2O molecules and OH^- ions during photocatalytic activity in an aqueous phase and adsorbed oxygen is reduced by electrons, $OH^{\bullet}$ and $O_2^{\bullet -}$ radicals are produced. Compared to the commonly utilized oxidants H_2O_2 and O_3, they are good oxidants. Complete oxidation occurs as a result of OH oxidants' repeated attacks on organic pollutants. There are two ways that $OH^{\bullet}$ is produced. First is the reduction of oxygen into O_2^- oxygen, which is then changed into $^{\bullet}OOH$ by attack of hole. Second, by oxidizing OH, $OH^{\bullet}$ is produced.[52,53] Rhodamine B dye is degraded by these radicals into harmless products like CO_2 and H_2O (Fig. 11).

The following is a presentation of the suggested mechanism of the synthesized samples:

$$\text{Composite} + h\nu \rightarrow \text{composite } (e^-/h^+)\text{@MXene} \quad (9)$$

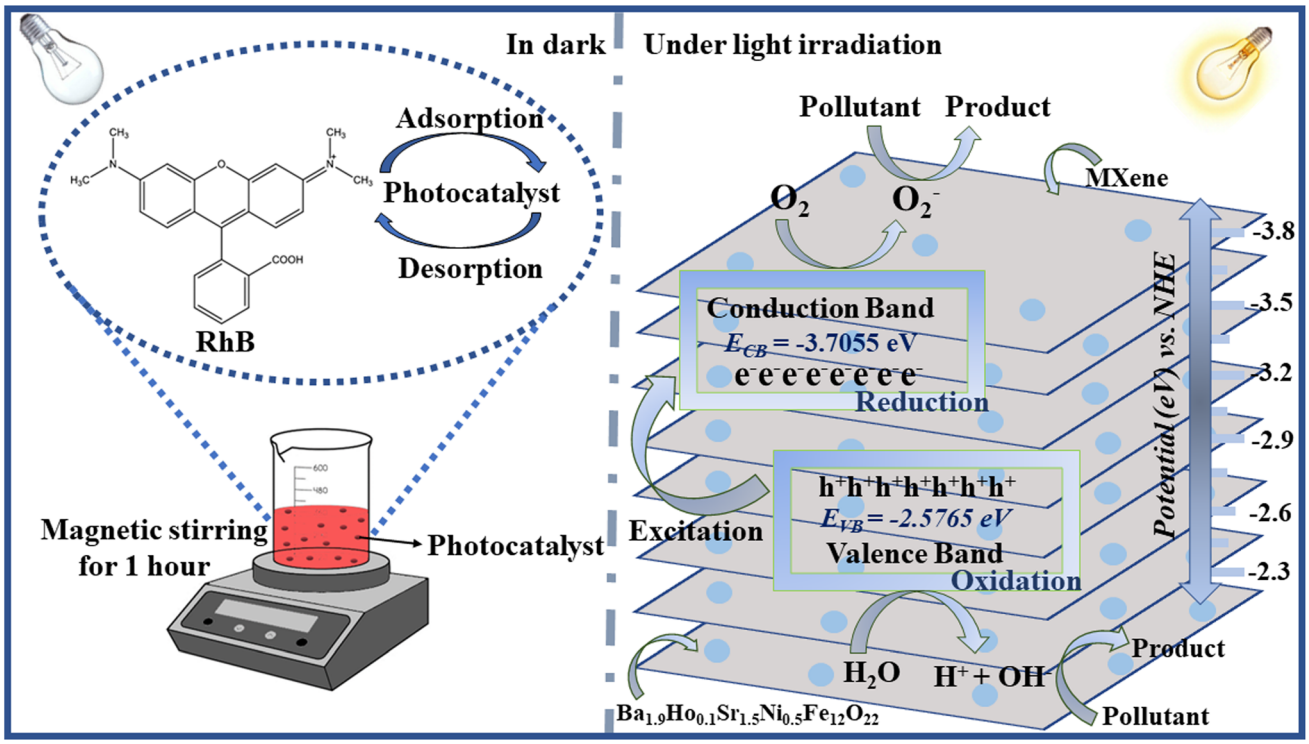

Fig. 11 Schematic diagram of photodegradation using synthesized samples.

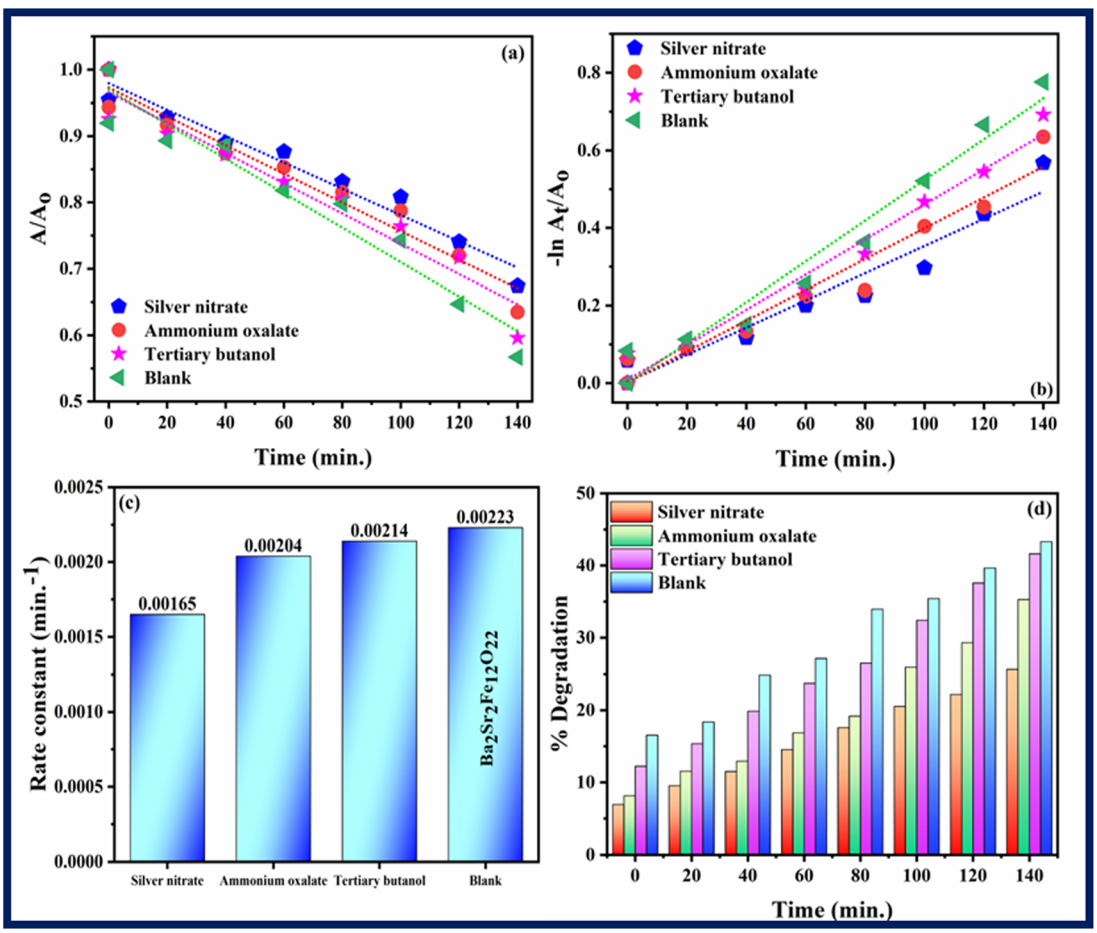

Fig. 12 (a and b) Kinetics plots, (c) rate constants plot (d) % degradation related to RhB dye degradation using $Ba_2Sr_2Fe_{12}O_{22}$ using different scavengers.

$$\text{Composite } (e^-/h^+)@\text{MXene} \rightarrow \text{composite } (h^+)@\text{MXene } (e^-) \quad (10)$$

$$\text{MXene } (e^-) + O_2 \rightarrow O_2^{2-*} + \text{MXene} \quad (11)$$

$$O_2^{2-*} + \text{RhB} \rightarrow \text{degradation products} \quad (12)$$

$$\text{Composite } (h^+) + OH^- \rightarrow \text{composite} + OH^* \quad (13)$$

$$OH^* + \text{RhB} \rightarrow \text{degradation products} \quad (14)$$

$$\text{MXene } (h^+) + \text{RhB} \rightarrow \text{degradation products} \quad (15)$$

There are two potential causes for the enhanced photoactivity of synthesized composite materials. Doping of holmium and nickel in $Ba_2Sr_2Fe_{12}O_{22}$ and composite with MXene decreases agglomeration and increases specific surface area. A greater specific surface area often yields a better harvesting efficiency of light. MXene sheets trap electrons and increase the charge carrier separation. Second, distinct redox energy levels of doped semiconductor made it easier for influentially separated photogenerated e^-/h^+ pairs to form, lengthening the life of charge carriers. According to the aforementioned findings, bare $Ba_2Sr_2Fe_{12}O_{22}$ is less active than $Ba_{1.9}Ho_{0.1}Sr_{1.5}Ni_{0.5}Fe_{12}O_{22}$@MXene composite.[54]

6. Scavenging experiment

Scavenging experiment was performed to investigate the main active species which are responsible for photodegradation of rhodamine B. Scavenging experiment was also carried out in similar conditions and procedure as followed in photocatalysis. Silver nitrate, ammonium oxalate, and tertiary butanol were taken as scavengers for quenching electrons (e^-), holes (h^+) and hydroxyl radicals (OH*), respectively.[55] Fig. 12–14 show results of scavenging experiment using $Ba_2Sr_2Fe_{12}O_{22}$, $Ba_{1.9}Ho_{0.1}Sr_{1.5}Ni_{0.5}Fe_{12}O_{22}$, and $Ba_{1.9}Ho_{0.1}Sr_{1.5}Ni_{0.5}Fe_{12}O_{22}$@MXene. Fig. 12–14(a) and (b) showed kinetics graphs of scavenging experiment and Fig. 12–14(c) and (d) showed the rate constant values and variation in % photocatalytic degradation of RhB by all three samples using these scavengers. The results of this experiment showed that electrons and holes were the main active species

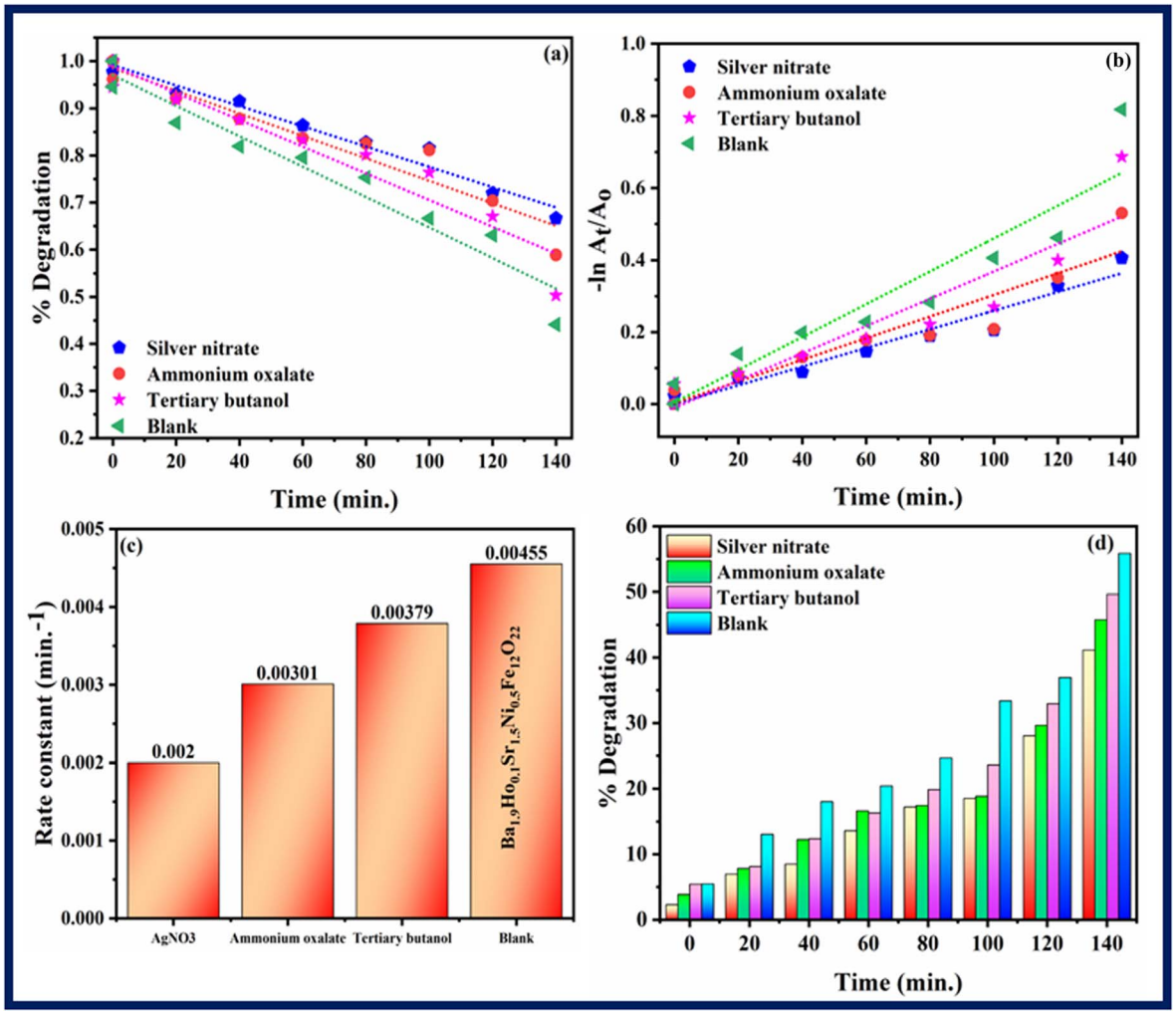

Fig. 13 (a and b) Kinetics plots, (c) rate constants plot (d) % degradation related to RhB dye degradation using $Ba_{1.9}Ho_{0.1}Sr_{1.5}Ni_{0.5}Fe_{12}O_{22}$ using different scavengers.

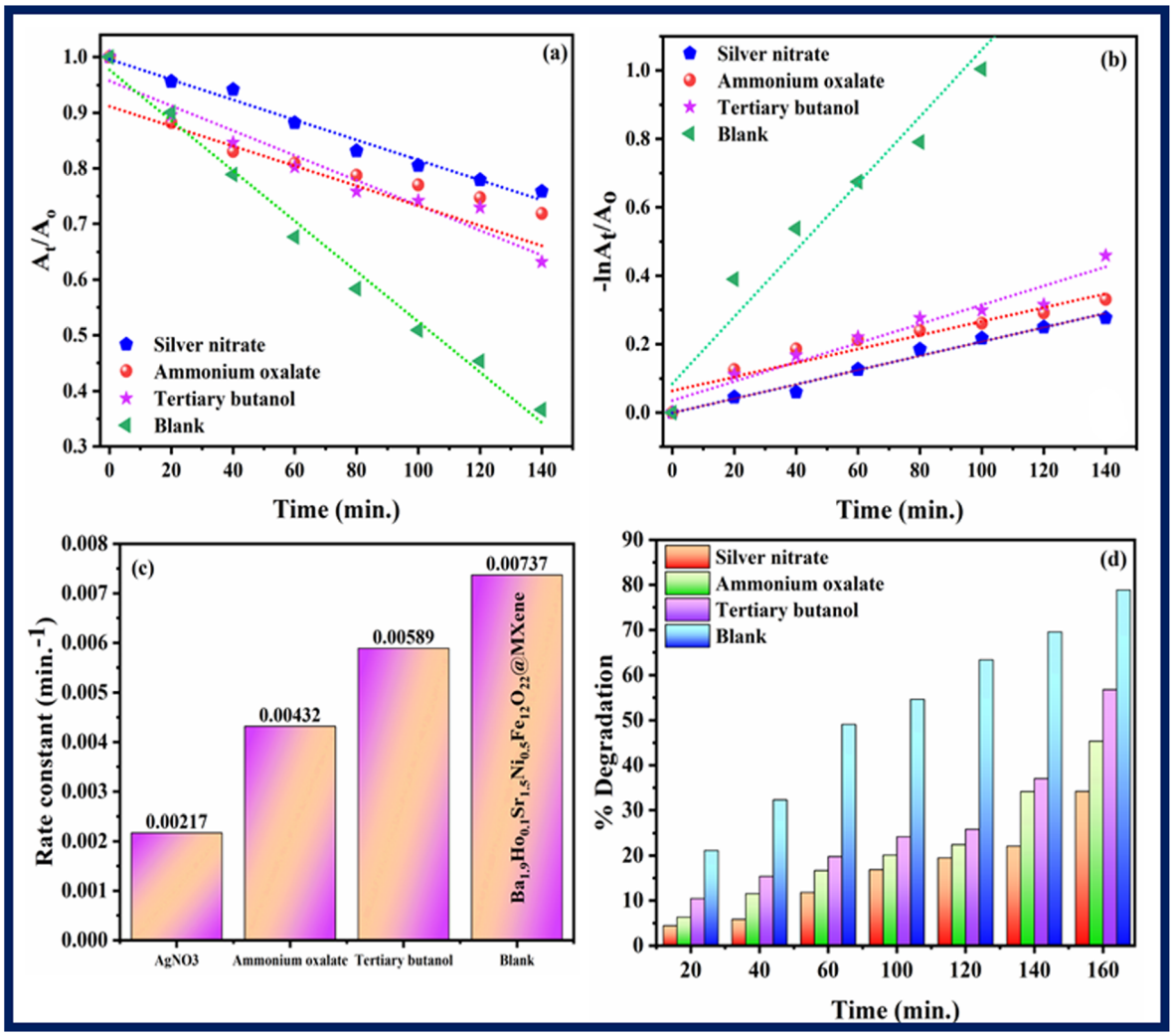

Fig. 14 (a and b) Kinetics plots, (c) rate constants plot (d) % degradation related to RhB dye degradation using $Ba_{1.9}Ho_{0.1}Sr_{1.5}Ni_{0.5}Fe_{12}O_{22}$@MXene using different scavengers.

involved in photodegradation process while hydroxyl radicals showed the least contribution in photocatalytic activity of RhB by using synthesized samples. The order of active species involved in photocatalytic activity was:

Electrons > holes > hydroxyl radicals

7. Conclusion

$Ba_{2-x}Ho_xSr_{2-y}Ni_yFe_{12}O_{22}$ (x = 0, 0.1 and y = 0, 0.5) and composite with MXene was successfully fabricated by sol–gel and ultra-sonication method. Various properties such as crystallite size, volume, band gap *etc.*, were analysed using X-ray diffraction (XRD), Fourier transform infrared spectroscopy (FT-IR), Scanning Electron Microscopy (SEM), and UV-visible spectroscopy. $Ba_2Sr_2Fe_{12}O_{22}$ and $Ba_{1.9}Ho_{0.1}Sr_{1.5}Ni_{0.5}Fe_{12}O_{22}$ have average crystallite sizes of 19.26 nm and 14.46 nm, respectively. The average grain size of $Ba_2Sr_2Fe_{12}O_{22}$ and $Ba_{1.9}Ho_{0.1}Sr_{1.5}Ni_{0.5}Fe_{12}O_{22}$, was calculated using ImageJ software and found to be approximately 26.8 μm and 24.7 μm, respectively. $Ba_2Sr_2Fe_{12}O_{22}$ and $Ba_{1.9}Ho_{0.1}Sr_{1.5}Ni_{0.5}Fe_{12}O_{22}$ have indirect band gap 1.7 eV and 1.129 eV, respectively. Photocatalytic behaviour of synthesized samples was studied using rhodamine B dye and pendimethalin pesticide as model pollutants. Maximum photodegradation of dye and pesticide was observed *i.e.*, 78.88% and 75.59%, respectively under similar conditions using $Ba_{1.9}Ho_{0.1}Sr_{1.5}Ni_{0.5}Fe_{12}O_{22}$@MXene. Scavenging experiment revealed that electrons and holes were the main active species taking part in photodegradation process. $Ba_{2-x}Ho_xSr_{2-y}Ni_yFe_{12}O_{22}$@MXene composite can be used as a potential applicant in cleaning environment and removing pollutants.

Conflicts of interest

There are no conflicts of interest to declare for our manuscript being submitted to your journal.

Acknowledgements

The authors express their sincere gratitude to the Deanship of Scientific Research at the Islamic University of Madinah for the support provided to the Post-Publishing Program. Authors are also thankful to the Division of Physical Chemistry, Institute of Chemistry, BJ Campus, The Islamia University of Bahawalpur (Pakistan) and GCU-Faisalabad (Pakistan).

References

1 W. Ouyang, *et al.*, Optimization of typical diffuse herbicide pollution control by soil amendment configurations under four levels of rainfall intensities, *J. Environ. Manage.*, 2016, **175**, 1–8.
2 W. Gong, *et al.*, Abiotic reduction of trifluralin and pendimethalin by sulfides in black-carbon-amended coastal sediments, *J. Hazard. Mater.*, 2016, **310**, 125–134.
3 J. V. Rohit and S. K. Kailasa, Simple and selective detection of pendimethalin herbicide in water and food samples based on the aggregation of ractopamine-dithiocarbamate functionalized gold nanoparticles, *Sens. Actuators, B*, 2017, **245**, 541–550.
4 A. Shahnazi, M. R. Nabid and R. Sedghi, Synthesis of surface molecularly imprinted poly-o-phenylenediamine/TiO2/carbon nanodots with a highly enhanced selective photocatalytic degradation of pendimethalin herbicide under visible light, *React. Funct. Polym.*, 2020, **151**, 104580.
5 A. K. Al-Buriahi, *et al.*, Elimination of rhodamine B from textile wastewater using nanoparticle photocatalysts: a review for sustainable approaches, *Chemosphere*, 2022, **287**, 132162.
6 S.-M. Lam, *et al.*, Sunlight responsive WO3/ZnO nanorods for photocatalytic degradation and mineralization of chlorinated phenoxyacetic acid herbicides in water, *J. Colloid Interface Sci.*, 2015, **450**, 34–44.
7 H. M. Abo-Dief, *et al.*, Ternary metal oxide WO3 NiO ZnO nanoparticles and their composite with CNTs for organic dye photocatalytic degradation, *Ceram. Int.*, 2022, **48**(15), 22269–22277.
8 R. Sedghi, *et al.*, High-performance visible light-driven Ni-ZnO/rGO/nylon-6 & Ni-ZnO/rGO/nylon-6/Ag nanofiber webs for degrading dye pollutant and study their antibacterial properties, *J. Alloys Compd.*, 2017, **729**, 921–928.
9 K. Okumura, *et al.*, Magnetism and magnetoelectricity of a U-type hexaferrite Sr 4 Co 2 Fe 36 O 60, *Appl. Phys. Lett.*, 2011, **98**(21), 212504.
10 R. Srivastava and B. C. Yadav, Ferrite materials: introduction, synthesis techniques, and applications as sensors, *Int. J. Green Nanotechnol.*, 2012, **4**(2), 141–154.
11 R. Kausar, *et al.*, Investigation into the structural and magnetic features of nickel doped U-type hexaferrites prepared through sol–gel method, *J. Magn. Magn. Mater.*, 2022, **549**, 169054.
12 B. I. Kharisov, H. R. Dias and O. V. Kharissova, Mini-review: ferrite nanoparticles in the catalysis, *Arabian J. Chem.*, 2019, **12**(7), 1234–1246.
13 D. Lisjak, D. Makovec and M. Drofenik, Formation of U-type hexaferrites, *J. Mater. Res.*, 2004, **19**(8), 2462–2470.
14 M. Chandra Dimri, *et al.*, Magnetic properties and 57Fe NMR studies of U-type hexaferrites, *J. Magn. Magn. Mater.*, 2011, **323**(16), 2210–2213.
15 R. C. Pullar, Hexagonal ferrites: a review of the synthesis, properties and applications of hexaferrite ceramics, *Prog. Mater. Sci.*, 2012, **57**(7), 1191–1334.
16 R. Kausar, *et al.*, Investigation into the structural and magnetic features of nickel doped U-type hexaferrites prepared through sol–gel method, *J. Magn. Magn. Mater.*, 2022, **549**, 169054.
17 P. Roonasi and M. Mazinani, Synthesis and application of barium ferrite/activated carbon composite as an effective solar photocatalyst for discoloration of organic dye contaminants in wastewater, *J. Environ. Chem. Eng.*, 2017, **5**(4), 3822–3827.
18 S. S. Raut, *et al.*, Enhanced photocatalytic activity of magnetic BaFe12O19 nanoplatelets than TiO2 with emphasis on reaction kinetics, mechanism, and reusability, *Ind. Eng. Chem. Res.*, 2018, **57**(48), 16192–16200.
19 I. Bibi, *et al.*, Effect of doping on dielectric and optical properties of barium hexaferrite: photocatalytic performance under solar light irradiation, *Ceram. Int.*, 2021, **47**(22), 31518–31526.
20 F. Bibi, *et al.*, Evaluation of structural, dielectric, magnetic and photocatalytic properties of Nd and Cu co-doped barium hexaferrite, *Ceram. Int.*, 2021, **47**(21), 30911–30921.
21 S. Anandan, *et al.*, Photocatalytic degradation of 2,4,6-trichlorophenol using lanthanum doped ZnO in aqueous suspension, *Catal. Commun.*, 2007, **8**(9), 1377–1382.
22 C. V. Reddy, *et al.*, Ni-dopant concentration effect of ZrO2 photocatalyst on photoelectrochemical water splitting and efficient removal of toxic organic pollutants, *Sep. Purif. Technol.*, 2020, **252**, 117352.
23 M. Shaban, *et al.*, Ni-doped and Ni/Cr co-doped TiO2 nanotubes for enhancement of photocatalytic degradation of methylene blue, *J. Colloid Interface Sci.*, 2019, **555**, 31–41.
24 X. Liu, *et al.*, Effect of holmium doping on the structure and photocatalytic behavior of TiO2-based nanosheets, *J. Mater. Sci.*, 2014, **49**(23), 8063–8073.
25 J.-w. Shi, J.-t. Zheng and P. Wu, Preparation, characterization and photocatalytic activities of holmium-doped titanium dioxide nanoparticles, *J. Hazard. Mater.*, 2009, **161**(1), 416–422.
26 M. Minakshi, *et al.*, New insights into the electrochemistry of magnesium molybdate hierarchical architectures for high performance sodium devices, *Nanoscale*, 2018, **10**(27), 13277–13288.
27 A. Ihsan, *et al.*, A strategy to boost the electrochemical properties of Ag–Fe2O3 with intercalation of MXene hydrogel, *Ceram. Int.*, 2023, DOI: **10.1016/j.ceramint.2023.09.091**.
28 S. Munir, *et al.*, Exploring the influence of critical parameters for the effective synthesis of high-quality 2D MXene, *ACS Omega*, 2020, **5**(41), 26845–26854.

29 A.-Z. Warsi, *et al.*, Synthesis, Characterization, Photocatalysis, and Antibacterial Study of WO3, MXene and WO3/MXene Nanocomposite, *Nanomaterials*, 2022, **12**(4), 713.
30 S. K. Hwang, *et al.*, MXene: an emerging two-dimensional layered material for removal of radioactive pollutants, *Chem. Eng. J.*, 2020, **397**, 125428.
31 M. Naguib, *et al.*, 25th anniversary article: MXenes: a new family of two-dimensional materials, *Adv. Mater.*, 2014, **26**(7), 992–1005.
32 A. Hojjati-Najafabadi, *et al.*, Magnetic-MXene-based nanocomposites for water and wastewater treatment: a review, *J. Water Process Eng.*, 2022, **47**, 102696.
33 I. A. Alsafari, *et al.*, Synthesis, characterization, photocatalytic and antibacterial properties of copper Ferrite/MXene (CuFe2O4/Ti3C2) nanohybrids, *Ceram. Int.*, 2021, **47**(20), 28874–28883.
34 D. Bokov, *et al.*, Nanomaterial by Sol-Gel Method: synthesis and Application, *Adv. Mater. Sci. Eng.*, 2021, **2021**, 5102014.
35 S. M. Reda, Synthesis of ZnO and Fe2O3 nanoparticles by sol–gel method and their application in dye-sensitized solar cells, *Mater. Sci. Semicond. Process.*, 2010, **13**(5), 417–425.
36 A. Zaleska, Doped-TiO2: a review, *Recent Pat. Eng.*, 2008, **2**(3), 157–164.
37 A. Rasheed, *et al.*, ZrxCo0. 8− xNi0. 2− xFe2O4-graphene nanocomposite for enhanced structural, dielectric and visible light photocatalytic applications, *Ceram. Int.*, 2016, **42**(14), 15747–15755.
38 I. Desai, *et al.*, Synthesis and characterization of magnetic manganese ferrites, *Mater. Sci. Energy Technol.*, 2019, **2**(2), 150–160.
39 D. Ravinder, Far-infrared spectral studies of mixed lithium–zinc ferrites, *Mater. Lett.*, 1999, **40**(5), 205–208.
40 M. A. Iqbal, *et al.*, Ti3C2-MXene/Bismuth Ferrite Nanohybrids for Efficient Degradation of Organic Dyes and Colorless Pollutants, *ACS Omega*, 2019, **4**(24), 20530–20539.
41 M. Aadil, *et al.*, Superior electrochemical activity of α-Fe2O3/rGO nanocomposite for advance energy storage devices, *J. Alloys Compd.*, 2016, **689**, 648–654.
42 J. Song, *et al.*, Microwave electromagnetic and absorbing properties of Dy3+ doped MnZn ferrites, *J. Rare Earths*, 2010, **28**(3), 451–455.
43 M. Afaq, *et al.*, Large-scale sonochemical fabrication of a Co 3 O 4–CoFe 2 O 4@ MWCNT bifunctional electrocatalyst for enhanced OER/HER performances, *RSC Adv.*, 2023, **13**(28), 19046–19057.
44 K. Hussain, *et al.*, Study of structural, optical, electrical and magnetic properties of Cu2+doped Zn0.4Co0.6-xCe0.1Fe1.9O4 spinel ferrites, *Phys. B*, 2020, **584**, 412078.
45 M. Hashim, *et al.*, Manganese ferrite prepared using reverse micelle process: structural and magnetic properties characterization, *J. Alloys Compd.*, 2015, **642**, 70–77.
46 K. Qian, *et al.*, The influence of Nd substitution in Ni–Zn ferrites for the improved microwave absorption properties, *Ceram. Int.*, 2020, **46**(1), 227–235.
47 S. Debnath, *et al.*, X-ray diffraction analysis for the determination of elastic properties of zinc-doped manganese spinel ferrite nanocrystals (Mn0.75Zn0.25Fe2O4), along with the determination of ionic radii, bond lengths, and hopping lengths, *J. Phys. Chem. Solids*, 2019, **134**, 105–114.
48 B. Aslibeiki, Nanostructural, magnetic and electrical properties of Ag doped Mn-ferrite nanoparticles, *Curr. Appl. Phys.*, 2014, **14**(12), 1659–1664.
49 A. Farooq, *et al.*, Fabrication of Ag-doped magnesium aluminate/rGO composite: a highly efficient photocatalyst for visible light-driven photodegradation of crystal violet and phenol, *Phys. B*, 2023, **650**, 414508.
50 A. Irshad, *et al.*, Ag-doped FeCo2O4 nanoparticles and their composite with flat 2D reduced graphene oxide sheets for photocatalytic degradation of colored and colorless compounds, *FlatChem*, 2022, **31**, 100325.
51 K. Khan, *et al.*, Structural, electrical, and photocatalytic properties of Y-type hexaferrite/carbon dot composite, *J. Mater. Sci.: Mater. Electron.*, 2023, **34**(25), 1793.
52 H. M. Abo-Dief, *et al.*, Ternary metal oxide WO3.NiO.ZnO nanoparticles and their composite with CNTs for organic dye photocatalytic degradation, *Ceram. Int.*, 2022, **48**(15), 22228–22236.
53 A. Ihsan, *et al.*, NiFe2O4/ZnO nanoparticles and its composite with flat 2D rGO sheets for efficient degradation of colored and colorless effluents photocatalytically, *Opt. Mater.*, 2022, **134**, 113213.
54 S. H. U. Din, *et al.*, Ag-doped nickel ferrites and their composite with rGO: synthesis, characterization, and solar light induced degradation of coloured and colourless effluents, *Ceram. Int.*, 2022, **48**(11), 15629–15639.
55 X. Chen, *et al.*, Preparation of ZnO Photocatalyst for the Efficient and Rapid Photocatalytic Degradation of Azo Dyes, *Nanoscale Res. Lett.*, 2017, **12**(1), 143.